

Low- and high-mode separation of short wavelength turbulence in dithering Wendelstein 7-AS plasmas

N. P. Basse^{a)}

Association EURATOM-Risø National Laboratory, DK-4000 Roskilde, Denmark
and Ørsted Laboratory, Niels Bohr Institute for Astronomy, Physics and Geophysics,
DK-2100 Copenhagen, Denmark

S. Zoletnik

CAT-SCIENCE Bt. Detrekö u. 1/b, H-1022 Budapest, Hungary
and Association EURATOM—KFKI-RMKI, H-1125 Budapest, Hungary

M. Saffman

Department of Physics, University of Wisconsin, Madison, Wisconsin 53706

J. Baldzuhn, M. Endler, M. Hirsch, J. P. Knauer, G. Kühner, K. McCormick,
A. Werner, and the W7-AS Team

Association EURATOM—Max-Planck-Institut für Plasmaphysik, D-85748 Garching, Germany

(Received 12 November 2001; accepted 3 April 2002)

In this article measurements of small scale electron density fluctuations in dithering high confinement (H)-mode plasmas obtained by collective scattering of infrared light are presented. A scan of the fluctuation wavenumber was made in a series of similar discharges in the Wendelstein 7-AS (W7-AS) stellarator [H. Renner *et al.*, Plasma Phys. Control. Fusion **31**, 1579 (1989)]. The experimental setup and discharge properties are described. H_{α} -light observing an inner limiter was used to separate low confinement (L)- and H-mode phases of the plasma; the separated density fluctuations are characterized. It was found that L- (H-) mode fluctuations dominate at high (low) frequencies, respectively, and that they possess well-defined and distinguishable scaling properties. Wavenumber spectra for L- and H-mode measurements are calculated and fitted by power-laws and exponential functions. The separated measurements can be fitted with the same exponents in L- and H-mode. Correlations between the density fluctuations, the H_{α} -signal and magnetic fluctuations as measured by Mirnov coils were analyzed. Correlation calculations using 50 ms time windows (several dithering periods) with time lag steps of 100 μ s showed that all the fluctuating quantities are highly correlated and that the maximum correlation occurs for high frequency density fluctuations. Performing separate L- and H-mode correlations on a 20 μ s time scale between magnetic and density fluctuations leads to the result that the minimum correlation time scale in L-mode is of order 100 μ s, while no correlation exists for H-mode. © 2002 American Institute of Physics. [DOI: 10.1063/1.1481747]

I. INTRODUCTION

Understanding the mechanism controlling access to improved confinement regimes such as the high confinement (H)-mode¹ in fusion plasmas remains a puzzle only partially solved. The literature dealing with the possible connection between turbulence suppression and the low confinement (L)-H transition is extensive—a present candidate being $\mathbf{E} \times \mathbf{B}$ shear flow decorrelation²—but several important questions remain unanswered. This statement is also valid for the so-called “advanced tokamak scenarios,” such as internal transport barriers (ITBs)³ during reversed magnetic shear (RS) operation, the radiatively improved (RI) mode⁴ and quiescent double barrier (QDB)⁵ discharges.

Transport in fusion plasmas appears to possess an intermittent nature with associated bursts^{6,7} of fluctuations in several plasma parameters. Observing the details of these bursts might shed light on the underlying phenomena. It would be

especially interesting to examine the temporal and spatial scales of the turbulent structures involved: (i) The correlation and time delay between bursts in various quantities, (ii) the behavior of bursts on different spatial scales and (iii) the lifetime of the bursts. Concerning this last point, the paramount question is whether the fluctuations display a “Chinese boxes”⁸ type of correlation or if we can resolve the temporal scale with the available sampling rates. That is, the time resolution (20 μ s) has to be sufficient to determine the correlation time of the bursts ($\sim 100 \mu$ s). We define the correlation time to be the full-width at half-maximum (FWHM) of the cross correlation function.

The discharges analyzed to answer these questions were part of a predivertor investigation on Wendelstein 7-AS (W7-AS) concerning itself with obtaining good core confinement and high recycling at the limiter.⁹ W7-AS has ten inboard carbon-fiber-composite limiters, acting to define the outer boundary of the plasma. The shots were well suited for a comparison between L- and H-mode plasmas, since they had a quasi-steady-state dithering phase.¹⁰ Dithering means a fast

^{a)}Electronic mail: nils.basse@risoe.dk

switching between the two confinement states.

The primary tool used in the article is small scale electron density fluctuation measurements obtained by the CO₂ laser based collective scattering diagnostic installed on W7-AS.¹¹ The other main diagnostic is a Mirnov coil system which provides information on magnetic fluctuations. For previous work done correlating magnetic and density fluctuations in W7-AS, we refer the reader to Ref. 12. The results therein show that the quantities are correlated in a region extending from 70% of the normalized minor radius out to the last closed flux surface (LCFS).

In the previous paragraphs and throughout the article, we use the expression “correlation of fluctuations.” To prevent confusion, we wish to make it clear that we mean the correlation of fluctuation power or its rms amplitude averaged over certain time windows, typically 10–100 μ s. The measurements which we analyze for possible correlations were not sampled using a common clock (the different analog to digital converters, ADC’s, were not synchronized), therefore we will not analyze crosspower spectra.

We report on results from a “wavenumber scan,” where the probed wavenumber of the density fluctuations was varied in steps from 14 to 62 cm^{-1} in eight similar discharges. To the best of our knowledge, density fluctuations in dithering plasmas have never previously been investigated at such large wavenumbers.¹³ However, measurements at these wavenumbers have recently become of interest due to non-linear numerical simulations treating electron temperature gradient (ETG) driven turbulence.¹⁴ For certain conditions, these simulations show that transport due to ETG modes can constitute a significant part of the total transport.

We will show that there is indeed a very fast correlation between magnetic and density fluctuations in L-mode, the cross correlation having a FWHM of order 100 μ s. Further, we prove that these correlations are strongest for the smallest wavenumbers measured and that the frequency of the density fluctuations, where a maximum correlation is observed with respect to other fluctuating quantities, increases with wavenumber.

A secondary aim is the thorough characterization of L- and H-mode separated density fluctuation autopower spectra. Although spectral shapes varied appreciably between L- and H-mode, the frequency integrated autopower change was quite modest. The differences found between L- and H-mode behavior in W7-AS and comparable scattering measurements in tokamaks warrants a comparative analysis.

It is of central importance to realize that when we in this article mention L- and H-modes, these are occurring under dithering conditions. No statements are made concerning either stationary L-mode or edge localized mode (ELM)-free H-mode (H*-mode). Our work presented is first part of an effort to clarify if dithering can be viewed as collections of closely spaced ELMs. Whether the two are manifestations of a single mechanism could be determined by the following two steps:

- (i) We elaborate certain properties of the fluctuations by picking out only the H-mode part of a dithering phase,

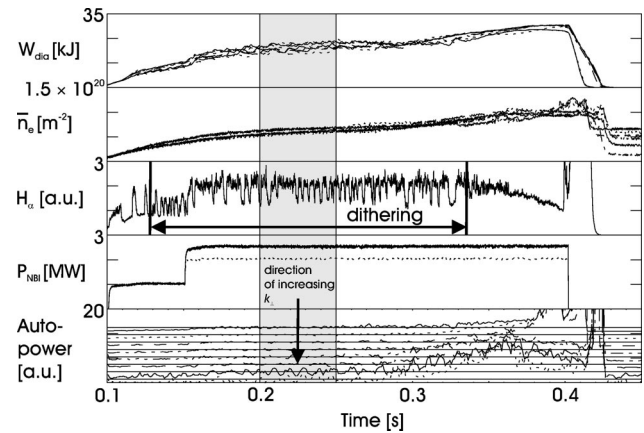


FIG. 1. Discharge overview-time traces from 100 to 450 ms. Linestyles in order of ascending wavenumber are solid, dotted, dashed, dash dot dot, and long dashes (cyclic usage). From top to bottom: diamagnetic energy (kJ), line density, H_{α} -light for shot 47133 (the dithering period is marked), NBI power (MW) and frequency integrated density fluctuations (1 ms time windows) in volume 1 normalized to the analysis time window (gray semi-transparent rectangle). The arrow on the density fluctuation data points in the direction of increasing wavenumber.

and show that these are clearly different from properties found by picking out only the ELM part of a dithering phase.

- (ii) We compare the results from the first step to an analysis of fluctuation properties in H*-mode and during individual (singular) ELMs.

In this article we address the first step; we treat the tasks belonging to the second step in a future publication.

The paper is organized as follows: In Sec. II we describe the discharges, the density fluctuation diagnostic and auxiliary diagnostics. Section III details the spectral characteristics of L- and H-mode separated density fluctuations. Section IV contains correlation analysis between H_{α} -light, magnetic and density fluctuations. In Sec. V we discuss and compare our findings to related tokamak measurements and finally we state our main conclusions in Sec. VI.

II. OVERVIEW

A. Discharge description

The discharges were separatrix limited with an edge rotational transform τ_a of 0.56 (the “ $\frac{5}{9}$ boundary island” configuration, where the main plasma is bounded by nine magnetic islands¹⁵) and had a duration of 400 ms.⁹ The deuterium plasmas were heated by hydrogen neutral beam injection (NBI) of up to 2.5 MW, where the absorbed power is about 75%. The discharges exhibited pronounced dithering; high NBI power was used to suppress the ELM-free H-mode.¹⁶ The effective plasma minor radius $r_{\text{eff}}(\text{LCFS})$ was 15 cm, with a toroidal magnetic field B_{ϕ} of 2.5 T and zero net current.

Figure 1 displays five time traces from 100 to 450 ms— from top to bottom: Diamagnetic stored energy, line density, H_{α} -trace for shot 47 133, NBI power and density fluctuations integrated over frequency for the eight discharges; top trace is the smallest wavenumber (length of time windows is 1

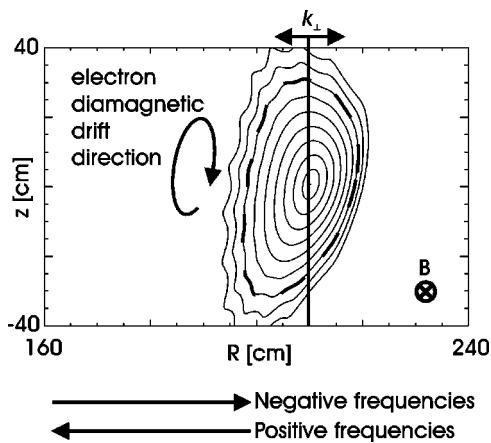


FIG. 2. Schematic drawing of the diagnostic setup on flux surfaces from a shot having a rotational transform of $\frac{1}{3}$. (The W7-AS equilibrium code TRANS could not calculate flux surfaces for the actual transform of $\frac{5}{9}$.) The dashed line shows the last closed flux surface due to limiter action. The magnetic field direction and corresponding electron diamagnetic drift direction is indicated. The measured wavenumber is along the major radius R .

ms). The fluctuations are normalized to the 50 ms time interval chosen for our main analysis, namely from 200 to 250 ms. The analysis time interval is represented by a gray semi-transparent rectangle in all figures containing quantities shown versus time (for additional time traces covering the analysis time window, see Fig. 7 below). Each trace is displaced for clarity, with horizontal lines marking the average values. The discharges had three phases: a startup phase to 150 ms, a quasi steady-state period from 150 to 300 ms and dynamical development from 300 to 400 ms where the discharges were terminated. The change of parameters at 300 ms is due to heavy gas puffing initiated at this point. Before this, the plasmas were exclusively fueled by the beams (total fueling $\sim 2.5 \times 10^{20} \text{ s}^{-1}$). It can be seen from the traces that the global plasma parameters in the analysis time window were roughly stationary. Note that one discharge (largest wavenumber) was heated by only 2 MW NBI.

B. The LOTUS diagnostic

The localized turbulence scattering (LOTUS) density fluctuation diagnostic has been described in detail elsewhere.¹¹ We will therefore limit ourselves to a rudimentary description below.

LOTUS is a dual volume diagnostic; two narrow (diameter $2w = 8 \text{ mm}$, where w is the beam waist) vertical measurement volumes toroidally displaced by 29 mm pass through the central plasma as indicated by the vertical line in Fig. 2. For additional information on the dual volume geometry we refer to Fig. 16 in Ref. 11. Each volume is formed by the crossing of a main (M) and local oscillator (LO) beam, the measured wavenumber (k_{\perp}) is determined by their cross-

ing angle. In the experiments analyzed herein the direction of k_{\perp} was set along the major radius R of the stellarator. Heterodyne detection is performed, meaning that we can distinguish the direction of the fluctuations as being due to inward (outward) [positive (negative) frequencies] traveling fluctuations parallel to R . The wavenumber can be varied from 14 to 62 cm^{-1} , which are extremely large values compared to similar diagnostics,^{17–19} but comparable to those of Ref. 20. The cited papers describe diagnostics measuring density fluctuation wavenumbers typically around 10 cm^{-1} . We will present measurements covering the entire wavenumber range in eight similar discharges. Due to the narrow volume waist (wavenumber resolution $\Delta k_{\perp} = 2/w = 5 \text{ cm}^{-1}$) and the small scattering angle, the measurements presented are line integrals of the density fluctuations along the volumes. Therefore determination of the spatial location of the fluctuations is indirect and relies on assumptions and previous experience (see Refs. 11 and 21 for localized turbulence measurements and profiles, respectively). For reference, we summarize the corresponding shot/wavenumbers in Table I.

C. Complementary diagnostics

The two main diagnostics we use for direct comparisons to the density fluctuations are H_{α} -light signals and magnetic fluctuations measured by Mirnov coils.

1. H_{α} and magnetic fluctuations

A diode measuring the H_{α} -emission at an inner limiter is used in this article, see Fig. 1. The signal was sampled at 10 kHz (100 μs). The emission comes from neutral hydrogen entering the plasma, so the H_{α} -signal is a measure of recycling between the plasma and vessel surfaces (see, e.g., Ref. 22, Subsection 4.13). Therefore, the abrupt drop in the H_{α} -signal at the L-H transition is due to a fast reduction of recycling. This is interpreted as being connected to an edge transport barrier associated with improved confinement.²³

The Mirnov coil system used consists of 16 coils (called “MIR-1”) around the plasma²⁴ and measures fluctuations in the poloidal magnetic field B_{θ} . Simulations show that the signal in a single coil primarily originates from a 5 cm region in front of the coil.²⁴ Figure 3 (top) shows the calibrated signal from a monitor coil (“MIRTIM”) in T/s, while the bottom plot shows a spectrogram for this trace. The time resolution was 4 μs . The dithering manifests itself as switching in the magnetic fluctuations and consists of broadband bursts.²⁵ As the sampling rate was 250 kHz (Nyquist frequency 125 kHz), aliasing problems are to be expected since bursts are observed up to 125 kHz. These bursts have for our discharges been determined to have an inversion point just inside the LCFS by the use of soft x-ray cameras.²⁶ For a detailed explanation of how to find the pivot point, see Fig. 18 in Ref. 25. Mode analysis shows that the poloidal mode

TABLE I. Measured wavenumber for a given shot.

Shot no.	47 133	47 135	47 136	47 137	47 138	47 141	47 142	47 143
Wavenumber (cm^{-1})	14	21	28	34	41	48	55	62

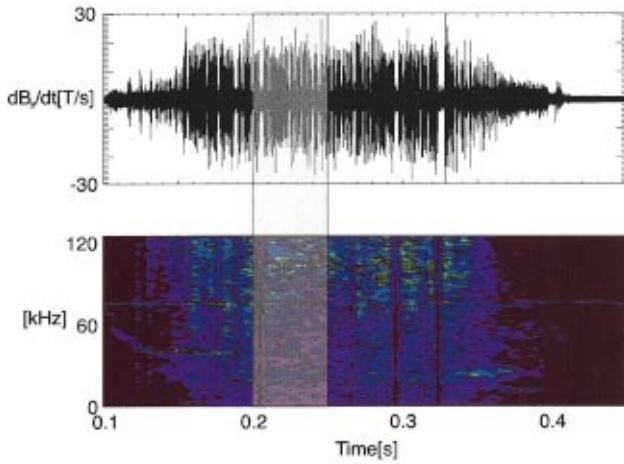


FIG. 3. (Color) Magnetic field derivative in T/s from the "MIRTIM" monitor coil (top) and a spectrogram (bottom) covering 350 ms. Dithering is observed as a large derivative.

numbers $m=2,3$ dominate during the bursts, while most of the mode activity disappears in the quiescent phases. A crude estimate of the perpendicular wavenumber of the perturbations is $k_{\text{MHD}} \sim m/r_{\text{MHD}} \sim 0.2 \text{ cm}^{-1}$, where r_{MHD} ($\sim 14 \text{ cm}$) is the minor radius location of the bursts. For the correlation calculations we use the rms signal of a coil situated at the midplane on the high field side of the plasma; the correlation calculations show that the coil selection is not important.

2. Spectroscopic measurements of the radial electric field

Measurements of the edge radial electric field E_r from shot 47 133 were obtained by passive spectroscopy using the 2824 Å boron IV line.²⁷ The electric field (using the lowest-order force balance equation) is given by

$$E_r = (v_\phi B_\theta - v_\theta B_\phi) + \frac{1}{eZ_I n_I} \nabla P_I, \quad (1)$$

where I is the common atomic species [see Ref. 27 for more elaborate formulas, Eqs. (9) and (10)]. Typically, the major contribution to E_r in W7-AS comes from poloidal rotation v_θ .²⁷

Figure 4 shows the edge E_r measured at five radial positions z in the edge plasma. The diagnostic coordinate z is about two times r_{eff} ; the measurement at $z=25 \text{ cm}$ is at the LCFS. The time resolution was 4 ms, which is not sufficient to resolve the fast switching between L- and H-mode. Therefore the figure shows data averaged over the 50 ms analysis time window.

We can convert E_r to $\mathbf{E} \times \mathbf{B}$ frequencies according to the relation

$$\omega_{E \times B} = 2\pi \nu_{E \times B} = k_\theta \frac{E_r}{B_\phi}, \quad (2)$$

where we use $k_\theta \sim k_\perp$.²⁸ A negative (positive) E_r means flow in the electron (ion) diamagnetic drift (d.d.) direction, respectively. It is seen that E_r towards the plasma edge is small and negative (zero within error bars), whereas it is large and

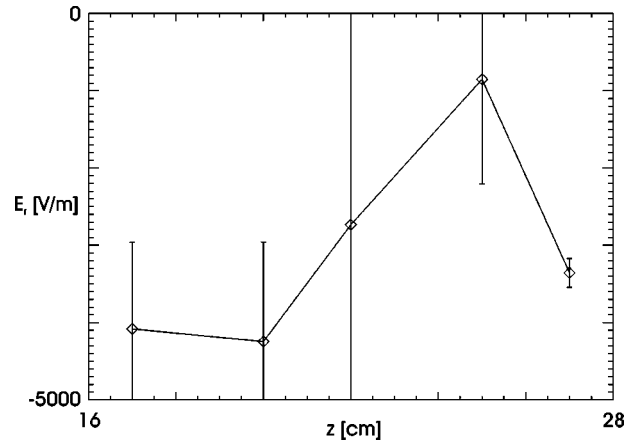


FIG. 4. Edge radial electric field E_r as determined by Boron IV spectroscopy versus z . The diagnostic coordinate z is roughly double the minor radius value.

negative inside the confined plasma. This would indicate that low frequencies rotate in the electron d.d. direction at the edge, high frequencies in the electron d.d. direction in the outer core. Using $E_r \sim -800$ (-4100) V/m for edge (outer core), we arrive at

$$\begin{aligned} \nu_{E \times B}^{\text{edge}}(14 \text{ cm}^{-1}) &= -71 \text{ kHz}, \\ \nu_{E \times B}^{\text{outer core}}(14 \text{ cm}^{-1}) &= -365 \text{ kHz}, \\ \nu_{E \times B}^{\text{edge}}(62 \text{ cm}^{-1}) &= -316 \text{ kHz}, \\ \nu_{E \times B}^{\text{outer core}}(62 \text{ cm}^{-1}) &= -1.6 \text{ MHz}. \end{aligned} \quad (3)$$

An important point with regards to E_r in the type of discharge we analyze is that it usually is quite small in the inner regions of the confined plasma, has a deep well (negative E_r) inside but close to the LCFS and a small hill (positive E_r) outside the LCFS. The measurements shown in Fig. 4 only display the outside slope of the well; the radial electric field at the bottom of the well is about -20 kV/m . An E_r profile for a discharge with profiles comparable to ours is shown as Fig. 6 in Ref. 27. In similar discharges having a lower dithering frequency (due to smaller NBI power), clear switching is established inside the LCFS, corresponding to a deepening of the E_r well in H-mode phases. The E_r inversion radius is, within errorbars, situated at the LCFS. The E_r is similar for the other discharges analyzed, resulting in a linear increase of the frequencies with k_\perp . In the following paragraphs dealing with profile measurements we will estimate the electron drift wave mode frequency to determine whether rotation or drift waves dominate our spectra.

3. Thomson scattering measurements of electron density and temperature

The final auxiliary measurements presented are electron density and temperature profiles (see Fig. 5). The measurements are made using a ruby laser Thomson scattering system that provides one density/temperature profile per discharge. We show profiles from three of our discharges, where the measurement time point was shifted between each discharge so as to provide the profile evolution. The red solid

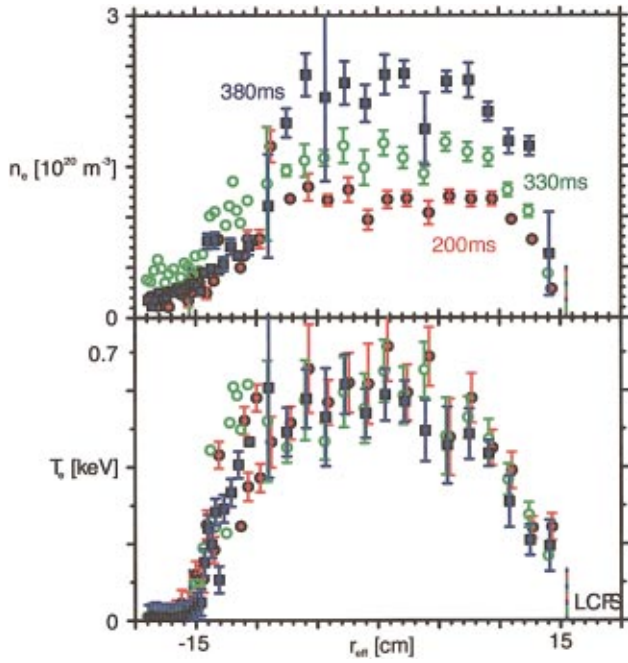


FIG. 5. (Color) Electron density (top) and temperature (bottom) profiles obtained using ruby laser Thomson scattering. Solid red dots are measured in shot 47 141 at 200 ms, open green dots in shot 47 138 at 330 ms and solid blue squares in shot 47 133 at 380 ms.

dots are taken at 200 ms, green open dots at 330 ms and blue solid squares at 380 ms. Our analysis interval begins at the 200 ms time point, where the central density was slightly above $1 \times 10^{20} \text{ m}^{-3}$, while the density rose to $2.5 \times 10^{20} \text{ m}^{-3}$ in the final stages. The central electron temperature was 0.6 keV.

Assuming a pure H plasma in our analysis time window (mass number $A = 1$) and an electron temperature of 0.3 keV (at $r_{\text{eff}} = 12 \text{ cm}$), the ion Larmor radius at the electron temperature ρ_s is equal to 1 mm. This means that the product $k_{\perp} \rho_s$ varies between 1.4 and 6.2 at the edge for the wavenumbers we are measuring, and is somewhat larger in the core. The profile information allows us to calculate estimates

of the linear mode frequency of electron drift waves, given by

$$\omega_e(k_{\theta}) = \omega_e^* \frac{1}{1 + k_{\theta}^2 \rho_s^2}, \tag{4}$$

$$\omega_e^* = - \frac{k_{\theta} T_e}{B_{\phi} L_n},$$

where $L_n^{-1} = |\partial_r \ln(n_e)|$ is the inverse electron density scale length.²⁹ We again assume that $k_{\theta} \sim k_{\perp}$ and we know that $L_n \sim 6 \text{ cm}$ from the density profile measurements. Thus, we conclude that

$$\begin{aligned} \nu_e^*(14 \text{ cm}^{-1}) &= -446 \text{ kHz}, \\ \nu_e(14 \text{ cm}^{-1}) &= -151 \text{ kHz}, \\ \nu_e^*(62 \text{ cm}^{-1}) &= -2.0 \text{ MHz}, \\ \nu_e(62 \text{ cm}^{-1}) &= -50 \text{ kHz}. \end{aligned} \tag{5}$$

In Sec. III we show that the measured density fluctuation frequencies extend up to 2 MHz. Comparing the drift wave electron d.d. frequencies to the ones due to $\mathbf{E} \times \mathbf{B}$ rotation, we conclude that rotation and not drift wave modes is responsible for the major part of the observed frequency shift for large wavenumbers. But since the observed frequency is the sum

$$\nu_{E \times B} + \nu_e = \frac{k_{\theta}}{B_{\phi}} \left(\frac{E_r}{2\pi} - \frac{T_e}{L_n(1 + k_{\theta}^2 \rho_s^2)} \right), \tag{6}$$

it is possible that low frequency drift wave turbulence is rotating at the $\mathbf{E} \times \mathbf{B}$ velocity.

Although rotation is dominating the measured spectra for large wavenumbers, the situation at small wavenumbers is ambiguous. This is because $\lim_{k_{\theta} \rightarrow 0} \nu_e = \lim_{k_{\theta} \rightarrow \infty} \nu_e = 0$ whereas $\nu_{E \times B}$ increases linearly with k_{θ} .

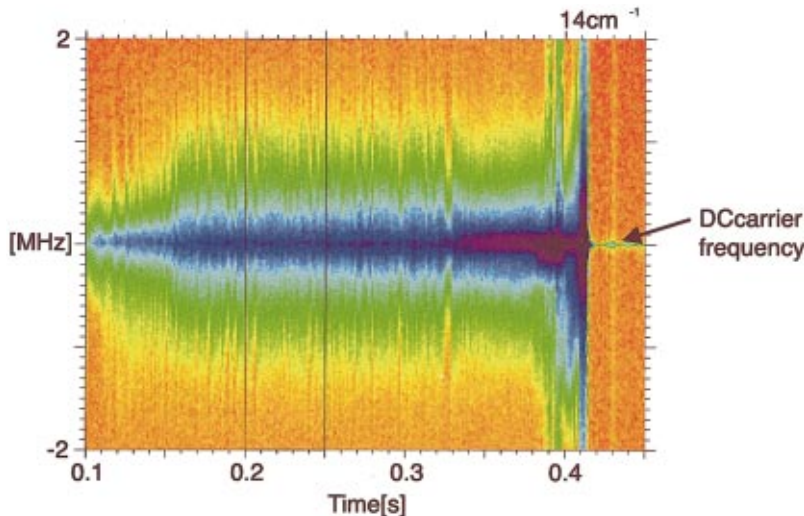


FIG. 6. (Color) Autopower versus time and frequency for discharge 47 133, volume 1. The time resolution of the spectra is 1 ms and the colorscale is logarithmic. The measured spectra in volume 2 are quantitatively similar to those in volume 1.

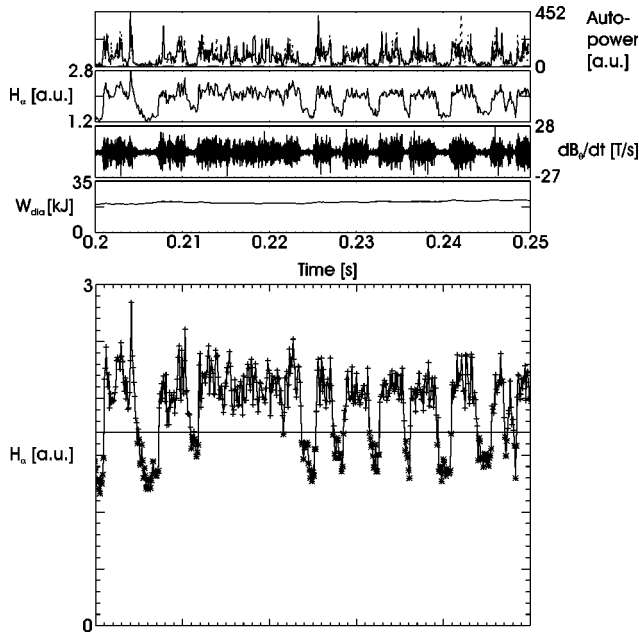


FIG. 7. Top to bottom: Density fluctuations at 700 kHz, $k_{\perp} = 14 \text{ cm}^{-1}$ in volumes 1 (solid) and 2 (dotted), H_{α} -light, magnetic fluctuations and the stored energy, separate bottom plot: H_{α} -trace for the same 50 ms time window. The horizontal threshold line selects L-mode (plusses) and H-mode (asterisks) time windows.

III. L- AND H-MODE SEPARATED AUTOPOWER SPECTRA

We begin our first analysis section with a brief introduction to the spectral analysis quantities we will use (Sec. III A). Thereafter we describe characteristics of the measured autopower spectra (Sec. III B), the behavior of the mean frequency (Sec. III C), and finally we present wavenumber spectra in Sec. III D.

A. Spectral analysis tools

The real signals acquired from each detector are centered at the heterodyne carrier frequency of 40 MHz. These are quadrature demodulated to obtain complex signals centered at zero frequency. The resulting signals are denoted

$$S_j(t) = X_j(t) + iY_j(t), \quad (7)$$

where j is the volume number (1 or 2). We can proceed and calculate

$$P_j(\nu) = \left| \int_{t_1}^{t_2} S_j(t) e^{-i2\pi\nu t} dt \right|^2, \quad (8)$$

the autopower spectrum of volume j for a time interval $\Delta t = t_2 - t_1$. The autopower in a certain frequency band $\Delta\nu = \nu_2 - \nu_1$,

$$P_j^b = \int_{\nu_1}^{\nu_2} P_j(\nu) d\nu, \quad (9)$$

is called the band autopower, as indicated by the lowercase superscript, b , in Eq. (9). The mean frequency is

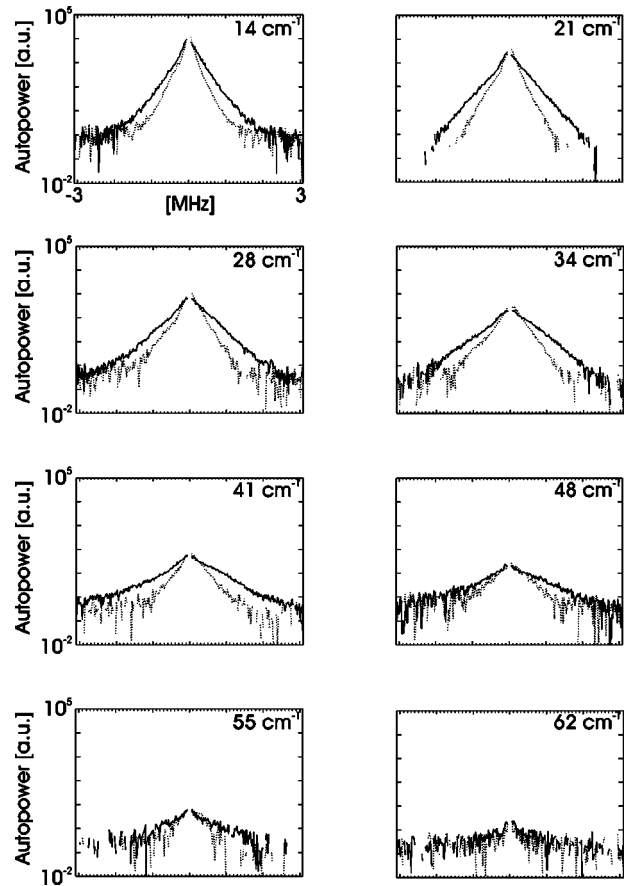


FIG. 8. Averaged autopower spectra for L-mode (solid) and H-mode (dotted) time windows.

$$\langle \nu \rangle_j = \frac{\int_{\nu_1}^{\nu_2} \nu P_j(\nu) d\nu}{\int_{\nu_1}^{\nu_2} P_j(\nu) d\nu}. \quad (10)$$

Finally, the power of the density fluctuations integrated over all frequencies where turbulence is observed is given by

$$P_j = \int_{-\nu_2}^{-\nu_1} P_j(\nu) d\nu + \int_{\nu_1}^{\nu_2} P_j(\nu) d\nu. \quad (11)$$

Note that the frequency interval $[-\nu_1, \nu_1]$ is excluded from the integrals; this is because the signal is dominated by the carrier frequency at low frequencies. In the following we use $\nu_1 = 50 \text{ kHz}$.

B. Autopower spectra

We begin our description of the density fluctuation autopower spectra by showing a spectrogram of shot 47 133 (volume 1) in Fig. 6. Density fluctuations are shown up to $\pm 2 \text{ MHz}$ on a logarithmic colorscale; the dc signal is our carrier frequency. The plot demonstrates our ability to obtain full spectral information over the entire discharge length. The L-H dithering shows as vertical lines and an increase in the autopower is observed as gas puffing commences around 300 ms.

To facilitate an immediate ‘‘correlation-by-eye,’’ the top four time traces of Fig. 7 show correlations between density fluctuations for a wavenumber of 14 cm^{-1} at 700 kHz,

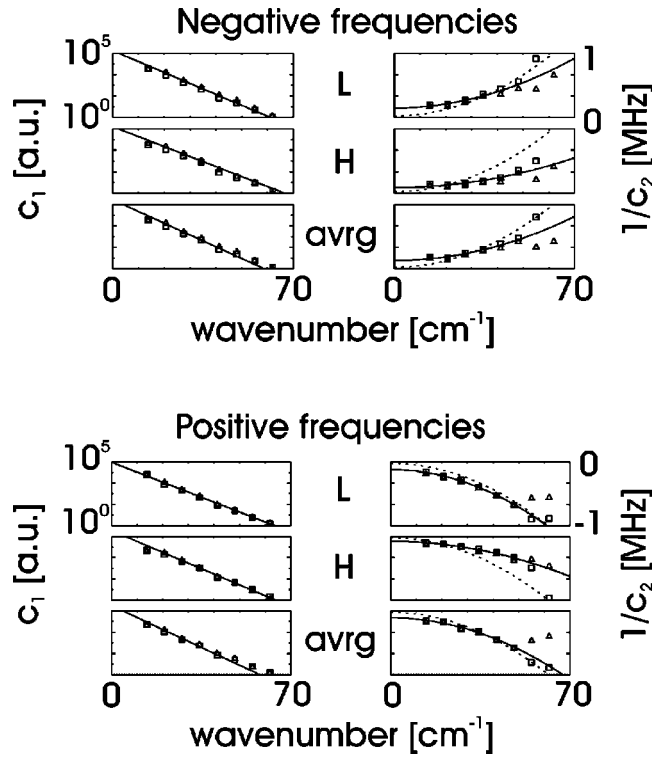


FIG. 9. Autopower fit coefficients for negative (three top rows) and positive (three bottom rows) frequencies. For each frequency sign: Left, top to bottom: c_1 vs k_\perp for L-mode, H-mode and average spectra. Right, top to bottom: $1/c_2$ vs k_\perp for L-mode, H-mode and average spectra. The solid lines on the left-hand sides are exponential fits to c_1 , while the right-hand solid lines are fits according to Eq. (14) (see text). The dotted lines are reference values from measurements in Alcator C (see text, Sec. III B). Triangles are volume 1, squares volume 2.

H_α -light and magnetic fluctuations. The stored energy is shown for reference at the bottom. The dithering observed is clearly long-time (ms) correlated (see Sec. IV A). That magnetic and density fluctuations are highly correlated is well known; see, e.g., Ref. 30 for a comparison between far-infrared (FIR) scattering and magnetic fluctuations. The separated bottom plot of Fig. 7 displays how we construct a series of L- and H-mode time windows from a time interval of 50 ms. A horizontal line delineates L-mode (plusses) and H-mode (asterisks) time points.

Constructing a series of L- and H-mode time windows as shown in Fig. 7 enables us to calculate autopower spectra of the density fluctuations for L- and H-mode plasmas separately: The autopower spectra are integrated over all L- or H-mode time intervals. This is illustrated in Fig. 8, where the

spectra are plotted for a single volume (1). Our initial observation is that the spectra all have a tent-like profile, which indicates that they might obey a

$$P(k_\perp, \nu) = c_1(k_\perp) \times e^{c_2(k_\perp)\nu} \quad (12)$$

type scaling,³¹ where P is autopower. This scaling is applied separately for positive and negative frequencies. Further, the H-mode spectra (dotted) are limited to lower frequencies than the L-mode spectra (solid) and are steeper as a function of frequency.

To get a better impression of the differences between the spectral shapes, Fig. 9 shows c_1 and $1/c_2$ along with the fits

$$c_1(k_\perp) = d_1 \times e^{-d_2 k_\perp} \quad (13)$$

and

$$c_2(k_\perp) = \frac{1}{d_3 [1 + (d_4/d_3) k_\perp^2]} \quad (14)$$

to negative (three top rows) and positive (three bottom rows) frequencies of the measured spectra shown in Fig. 8. The d 's are constants. The solid lines in the left-hand columns are exponential fits to c_1 , where the smallest wavenumber is excluded from the fit (to ensure convergence of the fit). The solid curves in the right-hand columns are fits to the data (excluding the two largest wavenumbers where the measurements are dominated by noise) assuming the dependency of Eq. (14), while the dotted curves (all identical) are results presented in Ref. 31 shown for reference. These reference fits were made to measurements of density fluctuations in the Alcator C tokamak. The fit coefficients are shown in Table II. Since d_3 and d_4 represent the slopes of the autopower spectra, we have directly shown that the H-mode slopes are much steeper than the corresponding L-mode ones. The average of the ratios

$$\left(\frac{d_3^L}{d_3^H} \right) \text{ and } \left(\frac{d_4^L}{d_4^H} \right) \quad (15)$$

for negative and positive frequencies is 1.8 ± 0.3 . This implies that if we “stretch” the H-mode frequency scale by this amount, the L- and H-mode slopes should be comparable. That this is indeed the case is shown in Fig. 10, where the H-mode frequencies are multiplied by 1.8. Or, stated in another fashion, the velocity of H-mode fluctuations is only about half the L-mode velocity.

TABLE II. The d fit coefficients. The subscripts refer to the frequency sign. Last column shows the result from Ref. 31.

Parameter	L_{neg}	H_{neg}	Average _{neg}	L_{pos}	H_{pos}	Average _{pos}	Reference
$d_1/10^5$ (a.u.)	1.6	1.5	2.4	0.9	2.9	2.6	...
d_2 (mm)	2.0	1.8	2.1	1.8	2.0	2.2	...
d_3 (kHz)	147	86	129	-121	-75	-108	22
d_4 (cm ² kHz)	0.159	0.094	0.140	-0.235	-0.113	-0.197	0.257
$\sqrt{d_4/d_3}$ (mm)	0.3	0.3	0.3	0.4	0.4	0.4	1.1

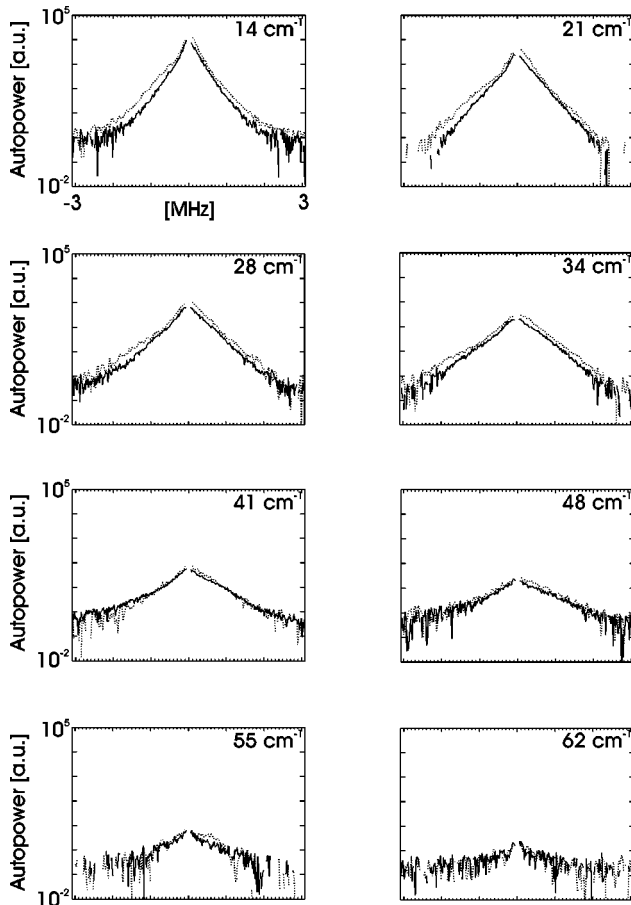


FIG. 10. Averaged autopower spectra for L-mode (solid) and H-mode (dotted) time windows. *Note:* The H-mode frequencies have been scaled by a factor 1.8 (see text, Sec. III B).

C. Mean frequencies

The velocity differences between L- and H-mode fluctuations can also be evaluated using mean frequencies. We show mean frequencies calculated separately for L- and H-mode time windows in Fig. 11. The results are shown for both negative and positive frequencies; the solid lines are fits

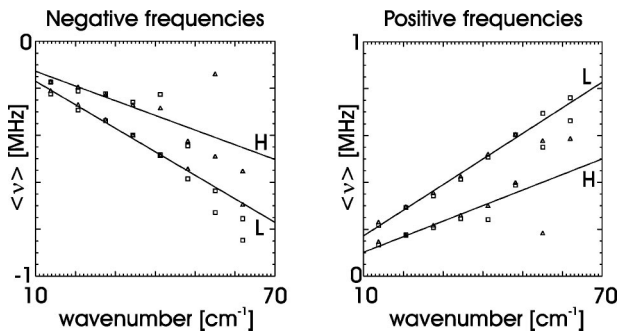


FIG. 11. Left: Mean frequency versus wavenumber for negative frequencies, right: for positive frequencies. The solid lines are fits assuming that the mean frequency scales linearly with wavenumber. Note that the L-mode slopes are larger than the H-mode slopes, and that the datapoints have a larger scatter above 50 cm^{-1} . Triangles are volume 1, squares volume 2.

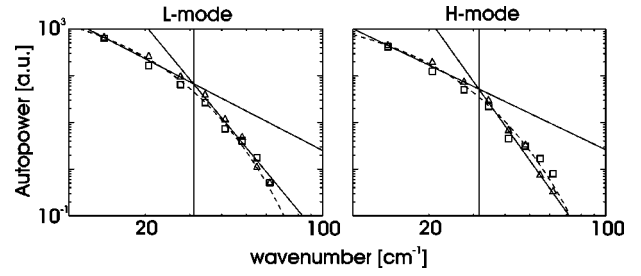


FIG. 12. Left: Wavenumber spectrum of L-mode density fluctuations, right: H-mode wavenumber spectrum. Solid lines are power-law fits to the three smallest and five largest wavenumbers, dashed lines are fits to exponential functions. The vertical lines indicate the transition wavenumber for the power-law fits. The power-law fit grouping of points used is the only one where convergence is obtained. Triangles are volume 1, squares volume 2.

to the datapoints assuming that the mean frequency scales linearly with wavenumber. The slope of the fits gives us mean velocities

$$\begin{aligned} \langle v \rangle_L &= 658 \pm 29 \text{ m/s}, \\ \langle v \rangle_H &= 405 \pm 12 \text{ m/s}, \end{aligned} \quad (16)$$

where the uncertainty estimate is constructed using frequencies of both signs. The ratio between the velocities is 1.6, slightly smaller than the value found in Sec. III B. If the mean velocities are exclusively due to a radial electric field, the size of this field would be

$$\begin{aligned} \langle E_r \rangle &= B_\phi \times \langle v \rangle, \\ \langle E_r \rangle_L &= 1.6 \text{ kV/m}, \\ \langle E_r \rangle_H &= 1.0 \text{ kV/m}, \end{aligned} \quad (17)$$

which is the typical E_r size at the plasma edge.

D. Wavenumber spectra

We now discuss separated L- and H-mode wavenumber spectra (see Fig. 12). The left-hand plot shows the frequency integrated L-mode power versus wavenumber, two power-law fits (solid lines) and an exponential function fit (dashed line). The right-hand side shows the H-mode frequency integrated power versus wavenumber, again fitted using power-laws or an exponential function. Two features are especially interesting here: (i) The L- and H-mode wavenumber spectra are similar, both in amplitude and as a function of wavenumber and (ii) either spectrum can be fitted using two power-laws or a single exponential function. Fits to power laws $P \propto k_\perp^{-m}$ give $m \sim 2.7$ at small wavenumbers and $m \sim 7$ at large wavenumbers (see also Refs. 32 and 19), whereas fits to exponential functions $P \propto e^{-nk_\perp}$ give $n \sim 0.15 \text{ cm}$ (fitting to the entire wavenumber range). Similar conclusions were reached in Tore Supra for ohmic and L-mode plasmas.³³ We again emphasize that these numbers are valid for *both* L- and H-mode.

To gauge the quality of the fits, one can calculate the reduced χ_ξ^2 for each fit, i.e., χ^2 normalized by the number of degrees of freedom ξ . For the power-law fits to small wavenumbers, $\chi_\xi^2 \sim 200$, which is very large compared to the expected value of 1. The power-law fits to large wavenumbers

give values close to 1, indicating a good quality fit. The exponential fits give $\chi^2_{\xi} \sim 10$, which is large but not compared to the small wavenumber power-law fits. To summarize, the exponential fits to all wavenumbers appear to offer the best compromise between small and large wavenumbers.

IV. CORRELATIONS

The temporal evolution of the autopower spectra indicated that (i) the amplitude of density fluctuations, magnetic field fluctuations and the H_{α} -signal changes in a correlated way at the L-H-L transitions. (ii) The time evolution of density and magnetic field fluctuations shows an intermittent nature (see Fig. 7). These phenomena will be analyzed in detail in the following subsections.

In this section we will focus on results obtained from density fluctuations in volume 1. The results from volume 2 have also been analyzed and were found to be qualitatively in agreement with the volume 1 results. Further, we only describe analysis made using positive frequencies from LOTUS; again, the results obtained from negative frequencies are analogous to the positive frequency results.

The quantities that are correlated below are density fluctuations from volume 1 having different frequencies, the rms power of Mirnov coil measurements and an H_{α} -signal. The Mirnov coil samples are $4 \mu\text{s}$ apart, so that 25 samples are used to construct the rms Mirnov power in Sec. IV A (100 μs time lag steps) and 5 samples are used in Sec. IV B to arrive at the 20 μs lag resolution.

A. Correlated changes in density fluctuations, limiter H_{α} -emission and magnetic fluctuation power

In this subsection we wish to quantitatively analyze the correlation between the limiter H_{α} -emission, density and magnetic field fluctuation amplitude by calculating cross correlations between these signals. The time lag resolution is limited by the H_{α} -signal, which is 100 μs . We will correlate time windows of 50 ms length, including several L- and H-mode phases. The objective is to establish that all the fluctuating fields are strongly correlated on this time scale. We begin by recalling the basic definitions: Usually, the cross covariance between two time series x and y is given as

$$R_{xy}(\tau) = \frac{1}{N} \sum_{k=0}^{N-\tau-1} (x_{k+|\tau|} - \bar{x})(y_k - \bar{y}) \quad \text{for } \tau < 0, \quad (18)$$

$$R_{xy}(\tau) = \frac{1}{N} \sum_{k=0}^{N-\tau-1} (x_k - \bar{x})(y_{k+\tau} - \bar{y}) \quad \text{for } \tau \geq 0,$$

where τ is time lag and N is the size of the two series.³⁴ Similarly, the cross correlation is conventionally defined in terms of cross covariances as

$$C_{xy}(\tau) = \frac{R_{xy}(\tau)}{\sqrt{R_{xx}(0) \times R_{yy}(0)}}. \quad (19)$$

We use this standard definition of the cross correlation in the present subsection, where the L- and H-mode separation is not done. We will in the next subsection describe modified

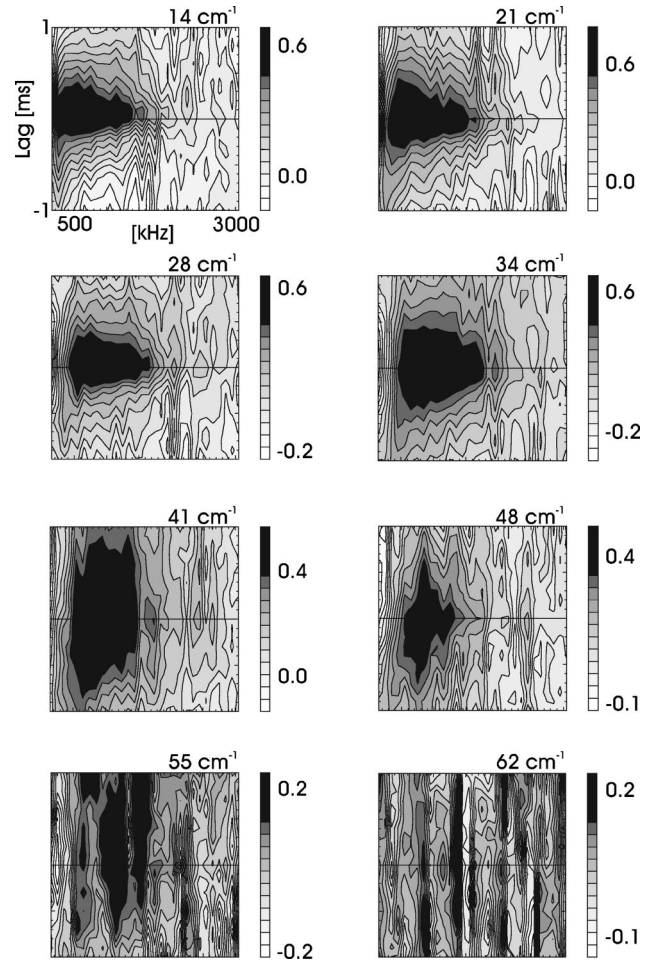


FIG. 13. Cross correlation between H_{α} and density fluctuation band autopower from collective scattering versus band central frequency and time lag (units of 100 μs). Note that the grayscale is different for each discharge.

versions of the correlations, designed to treat a series of time windows in order to calculate separate L- and H-mode correlations.

We will let the band autopower of the density fluctuations be the x series, and y be either the H_{α} -signal or the power of the Mirnov signal. This means that for positive lags, density fluctuations occur first, while for negative lags, they are delayed with respect to the other series. We will denote the lag where the correlation has a maximum the ‘‘toplag,’’ τ_0 .³⁵ The cross correlation will be calculated for several density fluctuation frequency bands and represented in contour plots; in these plots we define a global maximum correlation position in (τ, ν) -space: $\tau_0^{\max} = \text{MAX}(\tau_0)^b$.

We show two series of plots in Figs. 13 and 14. The contour plots show $C_{xy}(\tau)$ versus frequency of the density fluctuations and time lag in units of 100 μs (covering ± 1 ms lag in total).

Figure 13 shows the cross correlation between the density fluctuations and H_{α} for the discharge series analyzed. Our first observation is that τ_0^{\max} is close to zero time lag and displaced away from low frequency density fluctuations. For 21 cm^{-1} the correlation is largest, about 75%; it is clear that τ_0^{\max} shifts towards higher frequencies as the wavenumber is increased. The decay of the correlation is slower for positive

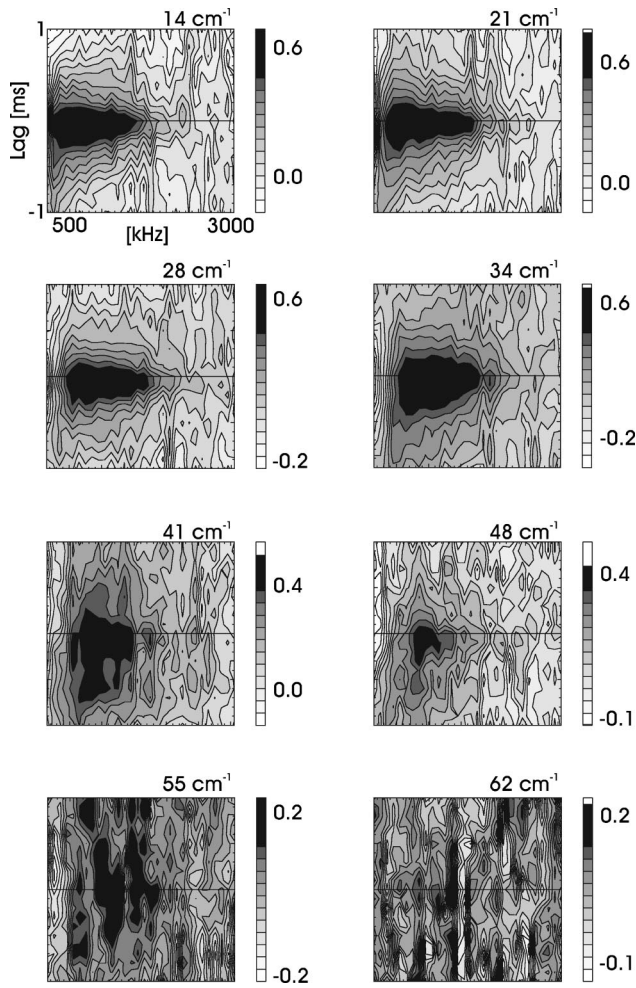


FIG. 14. Cross correlation between Mirnov rms signal and density fluctuation band autopower from collective scattering versus band central frequency and time lag (units of 100 μ s). Note that the grayscale is different for each discharge.

lags, where the H_α is delayed relative to the density fluctuations. This delay is due to the fact that the decay time of H_α in the L-H transition is hundreds of μ s, whereas the density fluctuations drop on a very fast time scale. So we have established that these two signals are highly correlated for small wavenumbers, that the correlation is lost for the largest wavenumbers and that there is a shift of τ_0^{\max} to higher frequencies with increasing wavenumber. On the 100 μ s time scale it is not possible to establish a time delay between the signals.

Figure 14 displays the cross correlation between the density fluctuations and the rms value of the magnetic fluctuations. Qualitatively, these plots are in agreement with what was found for the H_α -correlations, but now there is a small

systematic shift of the toplag to negative values; this indicates that the density fluctuations are somewhat delayed relative to the magnetic fluctuations. The time lag resolution is too coarse to conclude anything quantitative at this point—a rough estimate is a 100 μ s time delay. In Sec. IV B the analysis will be done using a faster time resolution. Finally, the shift of τ_0^{\max} towards higher frequencies for larger wavenumbers is also observed. The decay of the correlations is quite similar for lags of both signs.

B. Correlation between δn_e and $\partial_t B_\theta$ bursts

We saw in the previous subsection that the dithering itself is highly correlated, especially for small wavenumbers. To discover if the single spikes are correlated on an even faster time scale, we will separate the calculations to deal with either L- or H-mode time intervals. The intervals were selected as was described in Sec. III. Since we treat a number of L- and H-mode time windows, an averaging procedure must be made. In our notation, the number of L-mode time windows is N_L , where the length of L-mode window number n_L is equal to l_{n_L} (and equivalently N_H , n_H and l_{n_H} for H-mode). Two initial corrections to the cross covariance were made: (i) The normalization of the sum ($1/N$) was dropped and (ii) the averages used (\bar{x}_{tot} , \bar{y}_{tot}) were not simply averages of each time window, but averages over all time windows, L or H. This does not make a large difference since the overall time window is selected with care to be quasi-stationary. We denote the resulting cross covariances $R_{xy}^{\text{mod}}(\tau)_{j,m,n_m}$, where j is volume number (1 or 2) and m is mode designation (L or H):

$$R_{xy}^{\text{mod}}(\tau)_{j,m,n_m} = \sum_{k=0}^{l_{n_m}-\tau-1} (x_{k+|\tau|} - \bar{x}_{\text{tot}})(y_k - \bar{y}_{\text{tot}}) \quad \text{for } \tau < 0, \quad (20)$$

$$R_{xy}^{\text{mod}}(\tau)_{j,m,n_m} = \sum_{k=0}^{l_{n_m}-\tau-1} (x_k - \bar{x}_{\text{tot}})(y_{k+\tau} - \bar{y}_{\text{tot}}) \quad \text{for } \tau \geq 0,$$

where we have dropped the (j, m, n_m) subscripts on the right-hand sides for simplicity.

From the series of time windows we can construct an estimate of the mean cross covariance

$$\langle R_{xy}^{\text{mod}}(\tau)_{j,m} \rangle = \frac{\sum_{n_m=1}^{N_m} l_{n_m} R_{xy}^{\text{mod}}(\tau)_{j,m,n_m}}{\sum_{n_m=1}^{N_m} l_{n_m}}, \quad (21)$$

weighted by the length of the different time windows.³⁶ In analogy with this definition, we can construct a mean standard deviation

$$\langle \sigma(\tau)_{j,m} \rangle = \sqrt{\left(\frac{\sum_{n_m=1}^{N_m} l_{n_m} R_{xy}^{\text{mod}}(\tau)_{j,m,n_m}^2}{\sum_{n_m=1}^{N_m} l_{n_m}} - \langle R_{xy}^{\text{mod}}(\tau)_{j,m} \rangle^2 \right) \times \frac{1}{N_m - 1}} \quad (22)$$

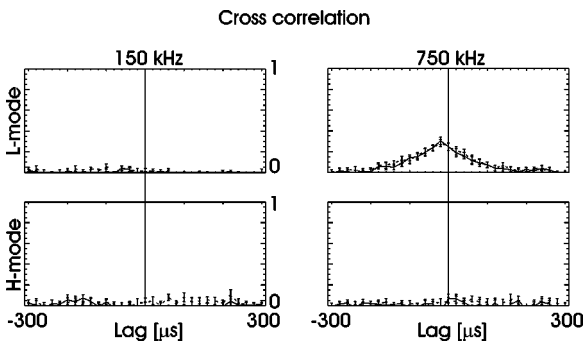


FIG. 15. Cross correlation between magnetic and density fluctuations for L- and H-mode time windows versus time lag (units of $20 \mu s$), 14 cm^{-1} . Left, cross correlation for 150 kHz density fluctuations, right for 750 kHz. Solid line is volume 1, dotted line volume 2.

to calculate approximate error bars on the correlations.

A corresponding procedure can be used for the cross correlation: We modify the cross correlation to arrive at $C_{xy}^{\text{mod}}(\tau)_{j,m,n_m}$ and take all time windows into account when averaging. The mean and mean standard deviation of the cross correlation is then found as was done for the cross covariance.

Having explained our procedure to calculate separated-cross covariances, cross correlations and error bars on these, we can proceed to the results. Figure 15 shows cross correlations between magnetic and density fluctuations for two frequencies, 150 kHz (left column) and 750 kHz (right column). The top plots show L-mode results, bottom H-mode. It is immediately apparent that neither L- nor H-mode fluctuations are correlated at low frequencies, whereas L-mode fluctuations are clearly correlated at higher frequencies. However, H-mode fluctuations remain uncorrelated. The L-mode high frequency toplag is slightly shifted towards negative lags (but at the limit of the lag resolution), indicating that the magnetic fluctuations occur about $20 \mu s$ before the density fluctuations. We must note that since the ADC's are not synchronized, systematic time delays could be due to electronic artifacts instead of actual time delays. The cross correlation in L-mode for high frequencies is seen to be 30%. This reduction in the cross correlation (compared to those in Sec. IV A) is due to the reduced signal-to-noise ratio arising from

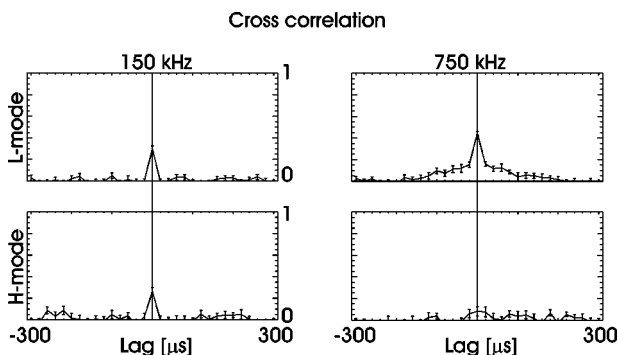


FIG. 16. Cross correlation between the density fluctuations in volumes 1 and 2 for L- and H-mode time windows versus time lag (units of $20 \mu s$), 14 cm^{-1} . Left, cross correlation for 150 kHz density fluctuations, right for 750 kHz.

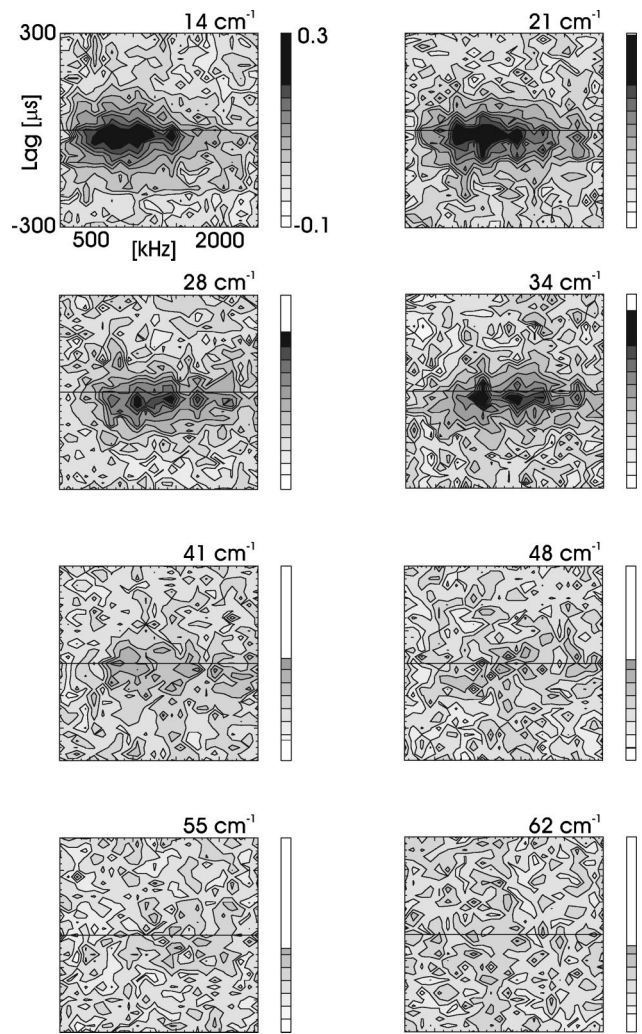


FIG. 17. Cross correlation between Mirnov rms signal and density fluctuation band autopower from collective scattering versus band central frequency and time lag for L-mode time windows (units of $20 \mu s$). The gray-scale on the right-hand sides of the plots shows what range of the total scale is relevant for the particular wavenumber.

the binning of fewer measurement points. The FWHM of the correlation is of order $100 \mu s$, which means that we have found the fastest time scales that are correlated. If the fluctuations had been correlated on even faster scales, we would only see a sharp peak of the correlation at one given lag.

Cross correlating a series of L- or H-mode time windows can also be applied to calculate the cross correlation between the density fluctuations measured in volumes 1 and 2 of LOTUS. An example for the same frequencies as those treated in the previous paragraph is shown in Fig. 16. At low frequencies, the fluctuations are correlated at zero time lag and have disappeared at $\tau = \pm 20 \mu s$. Our time resolution is in this case not sufficient to resolve the shape of the cross correlation. At higher frequencies, this feature disappears in H-mode, but remains in the L-mode cross correlation. Further, an additional broad shape emerges in the L-mode correlation and seems to be superimposed onto the narrow feature. This behavior persists for the discharges having larger wavenumbers.

We have now shown 2D plots of the results from one

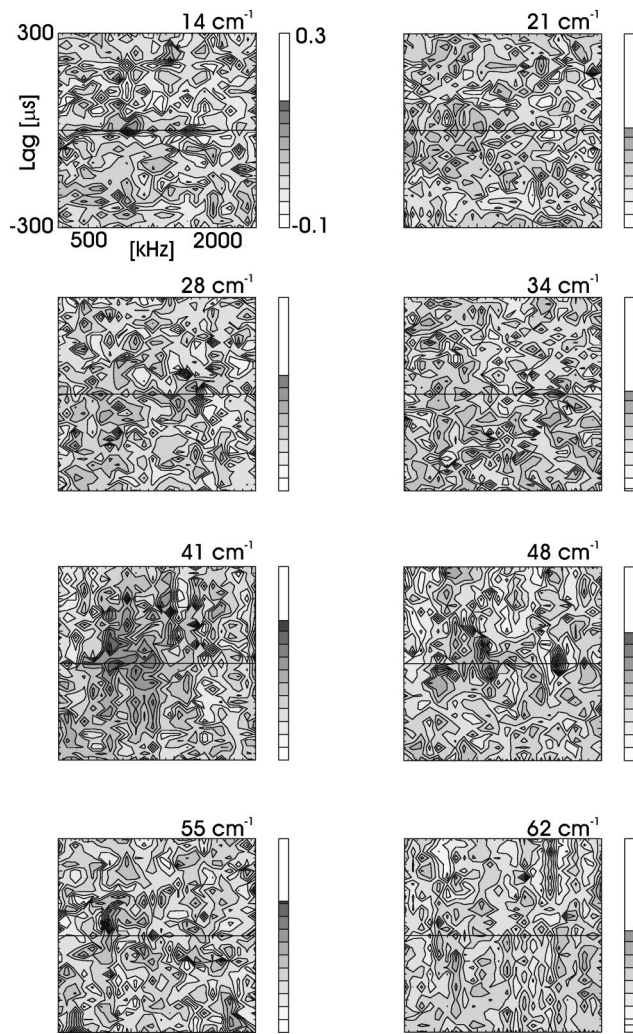


FIG. 18. Cross correlation between Mirnov rms signal and density fluctuation band autopower from collective scattering versus band central frequency and time lag for H-mode time windows (units of 20 μ s). The gray-scale on the right-hand sides of the plots shows what range of the total scale is relevant for the particular wavenumber.

shot at two frequencies (Fig. 15 left/right column). It is of course interesting to get the full picture, which can be accomplished by making 3D plots showing the L- and H-mode cross correlations versus density fluctuation frequency and time lag. These are shown for L-mode in Fig. 17 and H-mode in Fig. 18. Looking at the plots in Fig. 17, we see the same structure as was observed for the unseparated cross correlations: τ_0^{\max} is slightly shifted to negative lags, and towards higher frequencies. The global maximum correlation shifts to higher frequencies with increasing wavenumber, and disappears at the highest values. In contrast to these clear correlations, the H-mode case shown in Fig. 18 exhibits no clear correlation.

V. DISCUSSION

We have divided the discussion into two subsections: The analysis results presented in Secs. III and IV are discussed first, thereafter we describe measurements from the DIII-D tokamak and compare them to our findings.

A. W7-AS measurements

In this subsection discussing the W7-AS results, we treat measurements in the order they appear in the main text.

Our autopower spectra are all decreasing monotonically with frequency (Sec. III B). We note that this spectral shape has been observed in the FT-2 tokamak as well¹⁹ (for $k_{\perp} \geq 14 \text{ cm}^{-1}$), whereas pronounced “double hump” spectra peaking away from DC as observed in Tore Supra (see, e.g., Ref. 37) have not been observed in W7-AS, even with good spatial resolution.¹¹ The frequency range of the fluctuations does not increase substantially with wavenumber. This means that the phase velocity

$$v_{\text{ph}} = \frac{\omega}{k_{\perp}} \quad (23)$$

decreases with increasing wavenumber, i.e., smaller structures have a smaller phase velocity. Again, the same conclusion was reached in Ref. 19 and is thought to indicate that “the character of motion is different for fluctuations with different scale lengths.”

We found that the autopower slope versus frequency was steepest for H-mode phases, and that the L- and H-mode spectral shapes were close to identical if the H-mode frequencies were scaled by a factor 1.8. The trend of this observation was confirmed by the calculation of mean frequencies/velocities showing that the L-mode mean velocity was 1.6 times larger than the H-mode one (Sec. III C). This velocity decrease at the L-H transition could be caused by a decrease of $|E_r|$ at the radial position of the fluctuations. Usually the L-H transition is associated with a velocity increase at the plasma edge; these contradictory observations can be brought into agreement if the velocity decrease we observe is located deep inside the plasma. Alternatively, fluctuations could possess different characteristics than has previously been studied at the large wavenumbers we measure.

The small wavenumber power-law fit is quite close to the Kolmogorov value of $\frac{8}{3}$,³⁸ while the large wavenumber exponent is completely outside this range (Sec. III D). The fact that an exponential can fit all wavenumbers could mean that the wavenumbers observed are entering the dissipation range.³⁹ To determine whether there is a “hinge point” between two power-laws at a given scale or if the wavenumber spectrum is exponentially decaying we would need more than the eight datapoints used here. Converting the transition wavenumber for the power-law fits to a spatial scale gives $2\pi/k_{\perp} \sim 2 \text{ mm}$. The only natural spatial scale in the plasma close to this value is the ion Larmor radius, which is 1 mm. Wavenumber scans in plasmas having different hydrogen isotope ratios could clarify if the hinge point is connected to the ion Larmor radius. It is interesting to note that the found exponents apply to both L- and H-mode data, suggesting that the L-H transition does not change the relative weight of the fluctuation wavenumbers measured.

We have shown that high frequency density fluctuation bursts are strongly correlated with bursts in H_{α} -light and magnetic fluctuations on a sub ms time scale (Sec. IV A). In contrast, correlations are not observed at lower frequencies—this observation indicates that low and high frequency den-

sity fluctuations are two separate phenomena. Since the bursts associated with ELMy activity are known to originate a few centimeters inside the LCFS,¹⁶ it is likely that the high frequency density fluctuations are located here as well. The low frequency density fluctuations could be located somewhat outside the LCFS.¹¹ This would also be consistent with poloidal plasma rotation due to a large negative radial electric field E_r inside the LCFS and a small positive E_r outside. So, low frequency fluctuations (outside LCFS) are large in H-mode, while high frequency fluctuations (inside LCFS) are large in L-mode.

The separated L- and H-mode correlation analysis on a faster μs time scale showed that magnetic and density fluctuations are uncorrelated at low frequencies, but that L-mode high frequency density fluctuations are correlated to the magnetic fluctuations (Sec. IV B). H-mode fluctuations remain uncorrelated at high frequencies. We can think of two probable causes for the disappearance of high frequency correlations in going from L- to H-mode:

- (i) a reduction of the radial correlation length \mathcal{L}_r at the L-H transition (as has been quantified in, e.g., Ref. 40 using phase-contrast imaging), and
- (ii) that the fluctuating zone moves radially inwards.

The first option would be in agreement with $\mathbf{E} \times \mathbf{B}$ shear suppression theory and has been experimentally verified in DIII-D.

The second option would help to explain why a significant density fluctuation level remains, even in H-mode. However, this would contradict the claim that the low frequency fluctuations are to be found outside the LCFS where E_r is small. Therefore it could be the case that the low frequency fluctuations are deep inside the plasma, where E_r becomes small again.

B. Comparison with DIII-D measurements

We will in this subsection compare our results to those of the FIR scattering diagnostic installed on DIII-D.¹⁷ In the cited paper initial L-H transition observations were published; they showed that low frequency turbulence (up to a few hundred kHz) was suppressed in both poloidal directions, and that a high frequency feature in the ion d.d. direction appeared and gradually (over tens of ms) broadened in frequency during the H-mode (observations for $k_{\perp} = 5 \text{ cm}^{-1}$). The broadening was attributed to an increase of toroidal rotation.

The L-H transition in DIII-D has subsequently been described as a two-step process, where an initial zone of turbulence suppression (“shear layer”) having a radial extent of 3–5 cm just inside the separatrix is created within 1 ms.⁴¹ A further transport reduction on a 10 ms time scale is observed extending deeper into the confined plasma. The interior relative fluctuation level decreases about 50% during this period in comparison to the L-mode level.

A large positive E_r is observed in the core of DIII-D plasmas, attributed to toroidal rotation. The radial electric field decreases monotonically towards the edge, where a small negative E_r is found (mainly due to poloidal

rotation).⁴² The absolute value of E_r becomes larger after the L-H transition both inside and outside the LCFS, meaning that core (edge) fluctuations increase their ion (electron) d.d. direction. Assuming that $\mathbf{E} \times \mathbf{B}$ rotation dominates over turbulent mode frequencies, one can obtain localized information on the fluctuations.⁴³ This approach was used in Ref. 42 to conclude that the bulk of the fluctuations was localized at a normalized minor radius of 0.8.

The above paragraphs gave a brief overview of the L-H transition measurements from DIII-D. We will now relate these to the measurements from W7-AS. Let us begin by noting that our measurements deal with the fast initial suppression, since high NBI power is preventing the ELM-free H-mode. Therefore only features pertinent to the fast initial transition will be discussed.

The structure of E_r is quite different in DIII-D and W7-AS. We have in Sec. II C already described that the radial electric field in W7-AS has a deep well or small hill just inside or outside the LCFS, respectively. In comparable discharges where the dithering frequency is lower, the H-mode is associated with a deeper well inside the LCFS, while no clear development is seen outside the LCFS. This is in contrast to the DIII-D E_r structure described above, where the field both inside and outside the LCFS increases in magnitude.

If the conjecture that $\mathbf{E} \times \mathbf{B}$ rotation dominates is correct, changes in the E_r of W7-AS are consistent with the changes observed in the density fluctuation autopower spectra: As the plasma goes from L- to H-mode, the high frequency component is suppressed due to the deeper well inside the LCFS that increases the E_r shear. This agrees with the localization of an edge transport barrier in W7-AS that is situated within the first 3–4 cm inside the separatrix.⁴⁴ The low frequency component remains unchanged or increases slightly, probably due to a minor flattening of the hill outside the LCFS. Apparently, this explanation means that we can reconcile our measurements with those made with the DIII-D FIR diagnostic. We note for completeness that there is a possible ambiguity in the radial localization of the low frequency fluctuations, since a small E_r exists both outside the LCFS and deep in the confinement zone.

Comparing L- and H-mode autopower spectra⁴⁵ as we did in Fig. 8, a broadening of the spectrum was observed from L- to H-mode in DIII-D. This is interpreted as an indication of increased E_r shear. Although the spectrum widens, the frequency integrated power decreases markedly. This observation is the opposite of what we found in W7-AS, where the autopower spectra narrowed at the L-H transition.

A possible source for systematic differences between DIII-D and W7-AS measurements could be that fluctuations are reacting in a different fashion on varying spatial scales (DIII-D range [2, 16] cm^{-1} , W7-AS range [14, 62] cm^{-1}). The validity of this idea is difficult to test, but there are indications that electron transport remains anomalously large, also in the majority of improved confinement regimes.⁴⁶ Turbulence in the ITB gradient region has been attributed to the possible occurrence of ETG turbulence or other short wavelength modes.⁴⁷ A distinction can be made between small wavenumber ion temperature gradient (ITG)

turbulence and large wavenumber ETG turbulence.⁴⁸ This ordering is maintained in Ref. 49, where the increase of low frequency density fluctuations at the linear/saturated ohmic confinement (LOC/SOC) transition is argued to be due to long wavelength ($k_{\perp} \rho_s \approx 0.2 - 0.5$) ITG turbulence. Since the majority of present fluctuation diagnostics have an upper wavenumber limit of about 15 cm^{-1} ,^{17,50,51} a suppression of turbulence at these wavenumbers could still be consistent with turbulence remaining at larger wavenumbers. The usual observations are corroborated by reflectometry measurements at small wavenumbers in W7-AS;⁵² these demonstrate a large reduction of edge turbulence entering the quiescent H-mode in agreement with tokamak findings.

We briefly want to mention measurements of density fluctuations in DIII-D during negative central shear (NCS) operation.⁴⁶ A striking similarity between Fig. 3 in Ref. 46 (spectrogram of density fluctuation autopower versus time and frequency) and our Fig. 6 shows that the dithering signature in both cases consists of vertical lines in the plots (bursts of broadband frequency fluctuations). The transition from NCS L- to H-mode is accompanied by a fast drop in the low frequency edge fluctuations, while the high frequency core fluctuations are also reduced rather abruptly, but less pronounced in amplitude.

VI. CONCLUSIONS

The autopower results in Sec. III first of all demonstrate that ELMy or dithering behavior is seen in the density fluctuations at high frequencies, whereas the low frequency fluctuations do not display that connection. The overview Fig. 6 shows that the dithering activity manifests itself as high frequency bursts. We have further shown that the slope of the autopower spectra versus frequency can be described using an exponential function, and that the mean L-mode velocity is 1.6 times larger than the H-mode one. Low frequency turbulence remains present in H-mode plasmas, while high frequency structures are partially suppressed. From the assumption that the poloidal flow is dominated by the $\mathbf{E} \times \mathbf{B}$ Doppler shift we infer that low (high) frequencies originate outside (inside) the LCFS, respectively (Sec. V A). The persistence of low frequency turbulence in H-mode could be an indication that small scale turbulence is responsible for the anomalous electron transport that is observed even in H-mode plasmas. L- and H-mode separated wavenumber spectra can either be fitted to power laws or exponential functions, with almost identical exponents in both cases.

Our cross correlation analysis described in Sec. IV shows that the high frequency L-mode density fluctuations are correlated to the rms magnetic fluctuations, while this connection is not found for the H-mode phases. This could be explained by a reduction of the radial correlation length. Further, we have proven that there is a definite answer to our "Chinese boxes" question posed in the Introduction: Bursts are correlated on the $100 \mu\text{s}$ time scale, but not faster than that (Sec. IV B). The question remains whether the correlated structures are directly linked to global confinement.

The comparative analysis treating DIII-D and W7-AS measurements presented in Sec. V showed that density fluc-

tuations behave disparately in the two machines; in DIII-D the fast suppression of turbulence was observed at low frequencies, while the high frequencies were reduced in W7-AS. The probable explanation is the differing E_r , in that there is a well/hill structure in W7-AS and a monotonic field in DIII-D. Alternatively, the reason could be the different spatial scales observed.

Our investigations presented in this article on dithering plasmas will be augmented by an analysis of L- and ELM-free H-mode plasmas to be submitted for publication.

A radial injector currently being commissioned on W7-AS will provide us with the possibility to manipulate the radial electric field. This increased flexibility will be explored in future experiments to elucidate the interplay between turbulence and $\mathbf{E} \times \mathbf{B}$ shear.

ACKNOWLEDGMENTS

Useful discussions with the Risø plasma physics group, G. Antar, E. Holzhauser, and F. Volpe are gratefully acknowledged. Technical assistance by H. E. Larsen, B. O. Sass, J. C. Thorsen (Risø) and M. Fusseder, H. Scholz, and G. Zangl (Garching) was essential for the operation of LOTUS. N.P.B. wishes to thank P. Garrett, B. Hillman, R. Hirst, J. Moginie and M. Rotsey for continuing their essential work.

- ¹F. Wagner, G. Becker, K. Behringer *et al.*, Phys. Rev. Lett. **49**, 1408 (1982); V. Erckmann, F. Wagner, J. Baldzuhn *et al.*, *ibid.* **70**, 2086 (1993).
- ²H. Biglari, P. H. Diamond, and P. W. Terry, Phys. Fluids B **2**, 1 (1990); K. H. Burrell, T. N. Carlstrom, E. J. Doyle *et al.*, Plasma Phys. Controlled Fusion **34**, 1859 (1992); R. A. Moyer, K. H. Burrell, T. N. Carlstrom *et al.*, Phys. Plasmas **2**, 2397 (1995); E. J. Synakowski, Plasma Phys. Controlled Fusion **40**, 581 (1998); K. H. Burrell, Phys. Plasmas **6**, 4418 (1999); E. J. Synakowski, M. A. Beer, R. E. Bell *et al.*, Nucl. Fusion **39**, 1733 (1999); J. W. Connor and H. R. Wilson, Plasma Phys. Controlled Fusion **42**, R1 (2000).
- ³F. M. Levinton, M. C. Zarnstorff, S. H. Batha *et al.*, Phys. Rev. Lett. **75**, 4417 (1995); E. J. Synakowski, S. H. Batha, M. A. Beer *et al.*, *ibid.* **78**, 2972 (1997).
- ⁴A. M. Messiaen, J. Ongena, U. Samm *et al.*, Phys. Rev. Lett. **77**, 2487 (1996).
- ⁵C. M. Greenfield, K. H. Burrell, J. C. DeBoo *et al.*, Phys. Rev. Lett. **86**, 4544 (2001).
- ⁶E. Mazzucato, S. H. Batha, M. Beer *et al.*, Phys. Rev. Lett. **77**, 3145 (1996).
- ⁷Z. Lin, T. S. Hahm, W. W. Lee *et al.*, Phys. Rev. Lett. **83**, 3645 (1999).
- ⁸Chinese boxes; defined in Merriam-Webster's dictionary as Function: *noun plural*, Date: 1829, **1**: a set of boxes graduated in size so that each fits into the next larger one, **2**: something that resembles a set of Chinese boxes especially in complexity.
- ⁹K. McCormick, P. Grigull, J. Baldzuhn *et al.*, Plasma Phys. Controlled Fusion **41**, B285 (1999).
- ¹⁰H. Zohm, Phys. Rev. Lett. **72**, 222 (1994).
- ¹¹M. Saffman, S. Zoletnik, N. P. Basse *et al.*, Rev. Sci. Instrum. **72**, 2579 (2001).
- ¹²S. Zoletnik, M. Anton, M. Endler *et al.*, Phys. Plasmas **6**, 4239 (1999).
- ¹³S. Coda, M. Porkolab, and K. H. Burrell, Nucl. Fusion **41**, 1885 (2001).
- ¹⁴F. Jenko, W. Dorland, M. Kotschenreuther, and B. N. Rogers, Phys. Plasmas **7**, 1904 (2000).
- ¹⁵P. Grigull, K. McCormick, J. Baldzuhn *et al.*, Plasma Phys. Controlled Fusion **43**, A175 (2001).
- ¹⁶M. Hirsch, P. Grigull, H. Wobig *et al.*, Plasma Phys. Controlled Fusion **42**, A231 (2000).
- ¹⁷R. Philipona, E. J. Doyle, N. C. Luhmann, Jr. *et al.*, Rev. Sci. Instrum. **61**, 3007 (1990).
- ¹⁸A. Truc, A. Quéméneur, P. Hennequin *et al.*, Rev. Sci. Instrum. **63**, 3716 (1992).

- ¹⁹V. V. Bulanin, A. V. Vers, L. A. Esipov *et al.*, *Plasma Phys. Rep.* **27**, 221 (2001).
- ²⁰A. Boileau and J.-L. Lachambre, *Phys. Lett. A* **148**, 341 (1990).
- ²¹N. P. Basse, P. K. Michelsen, S. Zoletnik *et al.*, "Spatial distribution of turbulence in the Wendelstein 7-AS stellarator," *Plasma Sources Sci. Technol.* (in press).
- ²²J. Wesson, *Tokamaks* (Oxford University Press, Oxford, 1997).
- ²³F. Wagner, M. Keilhacker, and the ASDEX and NI Teams, *J. Nucl. Mater.* **121**, 103 (1984).
- ²⁴M. Anton, R. Jaenicke, A. Weller *et al.*, in *Proceedings of the 24th EPS Conference on Controlled Fusion and Plasma Physics*, ECA (European Physical Society, Petit-Lancy, 1997), Vol. 21A, p. 1645.
- ²⁵A. Weller, M. Anton, J. Geiger *et al.*, *Phys. Plasmas* **8**, 931 (2001).
- ²⁶A. Weller, private communication (2001).
- ²⁷J. Baldzuhn, M. Kick, and H. Maassberg, *Plasma Phys. Controlled Fusion* **40**, 967 (1998).
- ²⁸R. A. Koch and W. M. Tang, *Phys. Fluids* **21**, 1236 (1978).
- ²⁹C. X. Yu, D. L. Brower, S. J. Zhao *et al.*, *Phys. Fluids B* **4**, 381 (1992).
- ³⁰E. Holzhauser, G. Dodel, M. Endler *et al.*, *Plasma Phys. Controlled Fusion* **36**, A3 (1994).
- ³¹R. L. Watterson, R. E. Slusher, and C. M. Surko, *Phys. Fluids* **28**, 2857 (1985).
- ³²C. Honoré, R. Sabot, P. Hennequin *et al.*, in *Proceedings of the 25th EPS Conference on Controlled Fusion and Plasma Physics*, ECA (European Physical Society, Petit-Lancy, 1998), Vol. 22C, p. 647.
- ³³P. Hennequin, private communication (2001).
- ³⁴J. S. Bendat and A. G. Piersol, *Random Data: Analysis & Measurement Procedures* (Wiley, New York, 2000).
- ³⁵M. Zerbini, M. Austin, S. Bernabei *et al.*, *Plasma Phys. Controlled Fusion* **41**, 931 (1999).
- ³⁶P. R. Bevington and D. K. Robinson, *Data Reduction and Error Analysis for the Physical Sciences* (McGraw-Hill, New York, 1992).
- ³⁷J. Payan, X. Garbet, J.-H. Chatenet *et al.*, *Nucl. Fusion* **35**, 1357 (1995).
- ³⁸G. Antar, F. Gervais, P. Hennequin *et al.*, *Plasma Phys. Controlled Fusion* **40**, 947 (1998).
- ³⁹J. von Neumann, *Collected Works* (Pergamon, New York, 1963), Vol. VI, p. 437.
- ⁴⁰S. Coda, M. Porkolab, and K. H. Burrell, *Phys. Lett. A* **273**, 125 (2000).
- ⁴¹E. J. Doyle, R. J. Groebner, K. H. Burrell *et al.*, *Phys. Fluids B* **3**, 2300 (1991).
- ⁴²R. Philipona, E. J. Doyle, N. C. Luhmann, Jr. *et al.*, *Phys. Fluids B* **5**, 87 (1993).
- ⁴³C. L. Rettig, E. J. Doyle, W. A. Peebles *et al.*, *Rev. Sci. Instrum.* **66**, 848 (1995).
- ⁴⁴M. Hirsch, P. Amadeo, M. Anton *et al.*, *Plasma Phys. Controlled Fusion* **40**, 631 (1998).
- ⁴⁵C. L. Rettig, W. A. Peebles, K. H. Burrell *et al.*, *Nucl. Fusion* **33**, 643 (1993).
- ⁴⁶C. L. Rettig, W. A. Peebles, E. J. Doyle *et al.*, *Phys. Plasmas* **4**, 4009 (1997).
- ⁴⁷E. J. Doyle, G. M. Staebler, L. Zeng *et al.*, *Plasma Phys. Controlled Fusion* **42**, A237 (2000).
- ⁴⁸C. M. Greenfield, C. L. Rettig, G. M. Staebler *et al.*, *Nucl. Fusion* **39**, 1723 (1999).
- ⁴⁹C. L. Rettig, T. L. Rhodes, J. N. Leboeuf *et al.*, *Phys. Plasmas* **8**, 2232 (2001).
- ⁵⁰S. Coda and M. Porkolab, *Rev. Sci. Instrum.* **63**, 4974 (1992).
- ⁵¹P. Devynck, X. Garbet, C. Laviron *et al.*, *Plasma Phys. Controlled Fusion* **35**, 63 (1993).
- ⁵²M. Hirsch, E. Holzhauser, J. Baldzuhn *et al.*, in *Proceedings of the 16th IAEA Conference on Fusion Energy* (International Atomic Energy Agency, Vienna, 1996), Vol. 2, p. 315.